

Topological Charge of Soft X-ray Vortex Beam Determined by Inline Holography

Yuta Ishii (✉ yuta.ishii.c2@tohoku.ac.jp)

Tohoku University

Hironori Nakao

High Energy Accelerator Research Organization

Masaichiro Mizumaki

Japan Synchrotron Radiation Research Institute (JASRI/SPring-8)

Yusuke Wakabayashi

Tohoku University

Taka-hisa Arima

RIKEN Center for Emergent Matter Science

Yuichi Yamasaki

National Institute for Materials Science (NIMS)

Research Article

Keywords: Vortex Beam, Inline Holography, Topological

Posted Date: September 21st, 2021

DOI: <https://doi.org/10.21203/rs.3.rs-913911/v1>

License:  This work is licensed under a Creative Commons Attribution 4.0 International License.

[Read Full License](#)

Topological charge of soft X-ray vortex beam determined by inline holography

Yuta Ishii^{1,*}, Hironori Nakao², Masaichiro Mizumaki³, Yusuke Wakabayashi¹, Taka-hisa Arima⁴, and Yuichi Yamasaki^{2,4,5}

¹Department of Physics, Tohoku University, Sendai 980-8578, Japan

²Photon Factory, Institute of Materials Structure Science, High Energy Accelerator Research Organization, Tsukuba 305-0801, Japan

³Japan Synchrotron Radiation Research Institute (JASRI/SPring-8), Sayo 679-5198, Japan

⁴RIKEN Center for Emergent Matter Science (CEMS), Wako 351-0198, Japan

⁵Research and Services Division of Materials Data and Integrated System (MaDIS), National Institute for Materials Science (NIMS), Tsukuba, 305-0047, Japan

*yuta.ishii.c2@tohoku.ac.jp

ABSTRACT

A Laguerre–Gaussian (LG) vortex beam having a spiral wavefront can be characterized by its topological charge (TC). The TC gives the number of times that the beam phase passes through the interval $[0, 2\pi]$ following a closed loop surrounding the propagation axis. Here, the TC of soft X-ray vortex beams is determined using the in-line holography technique, where interference between vortex waves produced from a fork grating and divergent waves from a Fresnel zone plate is observed as a holographic image. The analyses revealed the phase distributions and the TC for the LG vortex waves, which reflects topological number of the fork gratings, as well as for the Hermite–Gaussian (HG) mode waves generated from the other gratings. We also conducted a simulation of the present technique for pair annihilation of topological defects in a magnetic texture. These results may pave the way for development of probes capable of characterizing the topological numbers of magnetic defects.

Introduction

Soft X-ray vortex beams, which have a spiral wavefront and finite orbital angular momentum, are expected to provide new tools for probing and/or manipulating the magnetic properties of materials, because of the high sensitivity of soft X-rays to the spin density of unoccupied states. Visible-light vortex beams have attracted intensive interest for decades¹, because of their various potential applications in, for example, optical tweezers² and super-resolution microscopy³ as well as the physics of optical induced excited states in magnetic materials^{4–6}. To bring new techniques to X-ray measurements, generation of X-ray vortex beams has been also investigated using undulators, spiral zone plates, and diffractive optics^{7–14}.

A possible practical application of soft x-ray vortex beams is as a probe for magnetic topological defects. Recently soft X-ray plane waves were reported to be transformed into vortex waves via an artificial spin lattice containing a topological defect¹⁵. Similarly, soft X-ray vortex beams are expected to be generated via topological defects in magnetic materials, such as magnetic Bloch points in helical or skyrmion lattices^{16–20}. These defects, especially their dynamics, have attracted much attention because of their potential applications in magnetic memory devices^{21,22}. Notably, the topological number of these defects, which reflects the winding number on the magnetic texture, can be transcribed to that of the vortex waves. Thus, detecting vortex beams generated from a topological defect would lead to effective magnetic probes for characterizing the topological features of magnetic textures. To this end, visualizing the spiral wavefront of a soft X-ray vortex beam and determining its topological number are critical, yet no technique has been established for this purpose.

Vortex waves can be expressed as a Laguerre–Gaussian (LG) mode²³ with an azimuthal wave function $\exp(i\ell\phi)$, where ϕ is the azimuthal angle in cylindrical coordinates. The parameter ℓ is the topological number, which is called the topological charge (TC); it represents the number of times that the beam phase passes through the interval $[0, 2\pi]$ following a closed loop C . It is given by

$$\ell = \frac{1}{2\pi} \oint_C \nabla\theta(\mathbf{r}) \cdot d\mathbf{r}, \quad (1)$$

where θ represents the phase distribution of the wave. In a recent study, we used soft X-ray inline holography experiments

(details of this technique are found in the second section) to visualize spiral phase for a soft X-ray vortex beams with $\ell = \pm 1$ produced from a fork grating (such as that shown in the inset of Fig. 1 (b)) with the topological number $b = 1$ ²⁴.

In the present study, we use the inline holography technique to determine the TC for various soft X-ray vortex waves generated from several types of gratings. The inline holography technique is also applied to a Hermite–Gauss (HG) X-ray mode, which can be used to produce LG and arbitrary polarization vortex modes²³. In addition, we present a simulation of using inline holography for pair annihilation of topological defects in a helical magnetic lattice.

Inline holography experiment and results

The experimental setup for inline holography is illustrated in Fig. 1 (a). Incident X-rays are first focused by a Fresnel zone plate (FZP), and the first-order diffraction waves from the FZP are selected by an order sorting aperture (OSA) placed at the focal point. Vortex waves generated as Bragg diffractions from the grating, which is positioned downstream of the focal point, interferes with the direct-beam waves from the FZP transmitting outside the grating. Recording the resultant interference patterns enables direct acquisition of phase information for the vortex waves.

The transmission of a fork grating with topological number b is expressed as¹³

$$t(\rho, \phi) = \frac{1}{2} \left(1 + \text{sgn} \left[\sin \left(\frac{2\pi}{d} \rho \cos \phi + b\phi \right) \right] \right), \quad (2)$$

in two-dimensional polar coordinates (ρ, ϕ) , where d is the pitch of the grating far from the center. The vortex beam with $\ell = nb$ is produced as the n -th Bragg diffraction from this grating. Here we performed inline holography for a fork grating with $b = 2$, which is illustrated in the inset of Fig. 1 (b). The LG states of n -th order Bragg diffraction from this fork grating can be ideally characterized by $\ell = nb = 2n$. Figure 1 (b) presents the interference pattern for $n = \pm 1$ diffraction waves from the fork grating positioned at $z_1 = 600 \mu\text{m}$ from the focal point and on the up-side of the annular transmitting waves from the FZP. The Holographic image was obtained using an CCD camera at $z_2 = 280 \text{ mm}$. Intensity modulation is observed along the horizontal direction, and the upper half of the diffraction pattern contains two additional stripes compared with the lower half, resulting in the appearance of two fork-shaped patterns around the center.

We used spatial frequency filtering to extract the phase distribution of these diffraction waves (details of the method are available in Ref.²⁴). The intensity for n th Bragg diffraction from a fork grating is calculated as²⁴

$$I_{nb}^{\text{inter}} \propto |\mathcal{J}'_{nb}| \sin \left\{ kR_2 + nb\phi_{fn} + \alpha_{nb} + n(b-1)\frac{\pi}{2} \right\}, \quad (3)$$

with

$$\mathcal{J}'_{nb}(\rho_{fn}) = \int_0^a e^{if_0\rho^2} \rho J_{nb}(\rho_{fn}\rho) d\rho \equiv |\mathcal{J}'_{nb}(\rho_{fn})| e^{i\alpha_{nb}}, \quad (4)$$

where (ρ_{fn}, ϕ_{fn}) are the local cylindrical coordinates with the center of the n th Bragg diffraction as the origin, and J_{nb} is the nb -th Bessel function of the first kind. The parameter R_2 represents the phase difference between the reference and diffraction waves and is expressed as

$$R_2 = \frac{z_1}{2z_2(z_2 - z_1)} \left\{ \left(x_2 - \frac{z_2}{z_1} x_g \right)^2 + \left(y_2 - \frac{z_2}{z_1} y_g \right)^2 \right\}, \quad (5)$$

with the center of the grating (x_g, y_g, z_1) and the detector plane (x_2, y_2, z_2) . The Fourier transform \mathcal{F} of the interference intensity is expressed as

$$\mathcal{F}(I) = G_{\text{DC}} + G_{\text{AC}+} + G_{\text{AC}-}, \quad (6)$$

where G_{DC} and $G_{\text{AC}\pm}$ are the DC and AC components of $\mathcal{F}(I)$, respectively. An interference term is included in $G_{\text{AC}\pm}$. Thus, the spiral phase distribution can be extracted by filtering $G_{\text{AC}+}$, applying an inverse Fourier transform \mathcal{F}^{-1} , and multiplying by the term $\exp(-ikR_2)$:

$$f(\rho_{fn}, \phi_{fn}) \equiv \exp(-ikR_2) \mathcal{F}^{-1}(G_{\text{AC}+}) \quad (7)$$

$$= A(\rho_{fn}, \phi_{fn}) \exp(inb\phi_{fn} + i\alpha_{nb}), \quad (8)$$

where $A(\rho_{fn}, \phi_{fn})$ is the amplitude of the vortex wave.

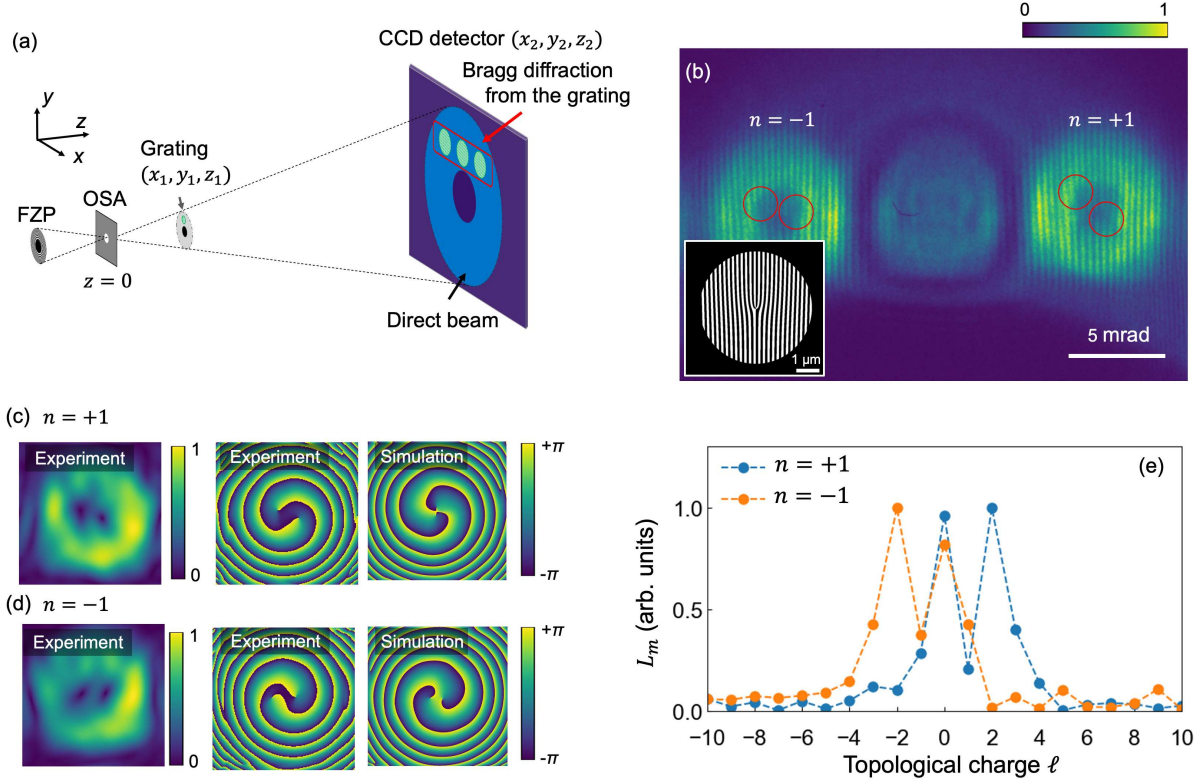


Figure 1. (a) Schematic of the experimental setup for soft X-ray inline holography. Incident X-rays are focused via a Fresnel zone plate (FZP). The first-order diffraction from the FZP is selected by an order sorting aperture (OSA) placed in the vicinity of the focal point. A grating placed downstream of the focal point produces Bragg diffraction waves, which interfere with direct waves transmitting outside the grating. The interference pattern is observed at the CCD detector as a holographic image. (b) Hologram pattern from the fork grating with $b = 2$ shown in the inset. Red circles indicate fork shaped patterns. (c)(d) $A(\rho_{fn}, \phi_{fn})$ (first column) and phase distribution (second column) of the vortex diffraction waves for (b) $n = +1$ and (c) $n = -1$, as obtained using spatial frequency filtering (refer to the main text). Figures in third column present simulated phase patterns for these vortex diffraction waves. (e) TC spectra for the $nb = \pm 2$ diffraction waves obtained using the method described in the main text.

$A(\rho_{fn}, \phi_{fn})$ and the phase distributions for the $nb = \pm 2$ diffraction waves are presented in the figures in the first and second columns of Figs. 1 (c) and (d). A double spiral phase distribution is obtained for each diffraction wave, and the angular rotation direction is reversed between them. In addition, Fermat's spiral-like patterns are observed, arising from the term of $\exp(i\alpha_{nb})$ ²⁴. Each phase pattern contains two singularities near the center, which indicates that a vortex beam with $\ell = 2$ splits into two vortex beams with $\ell = 1$. This phenomenon, known as charge splitting, is attributed to contamination of the $\ell = 0$ mode as a result of imperfection in the shape of the fork grating²⁵. We also simulated the phase distribution for these waves using the scaled fast Fourier transform (FFT) method²⁶. In this calculation, we assumed an ideal FZP and fork grating. The figures in the third column of Figs. 1 (c) and (d) show the simulated phase patterns, which reasonably reproduce the experimental results.

To extract the TC of the vortex waves, we calculated L_m expressed as

$$L_m \equiv \left| \int_0^{\rho_{\max}} \rho d\rho \int_0^{2\pi} d\phi f(\rho, \phi) \exp(-im\phi) \right|, \quad (9)$$

where ρ_{\max} reflects the size of the region which we took as the diffraction image (as shown in Figs. 1 (c) and (d)). L_m represents the decomposition to the $\ell = m$ mode of a vortex wave and thus gives the TC spectrum amplitudes. L_m includes the integral of $A(\rho_{fn}, \phi_{fn})$, which indicates that L_m is ideally independent of ρ_{\max} if ρ_{\max} is sufficiently large to include the diffraction peak, because $A(\rho_{fn}, \phi_{fn})$ is ideally zero outside the diffraction region. Figure 1 (e) shows the TC spectrum obtained for the $n = \pm 1$ diffraction waves. This spectrum shows well-defined peaks at $\ell = \pm 2$ for the $n = \pm 1$. In addition, an additional strong peak appears at $\ell = 0$ for both waves, clearly indicating contamination of the $\ell = 0$ mode.

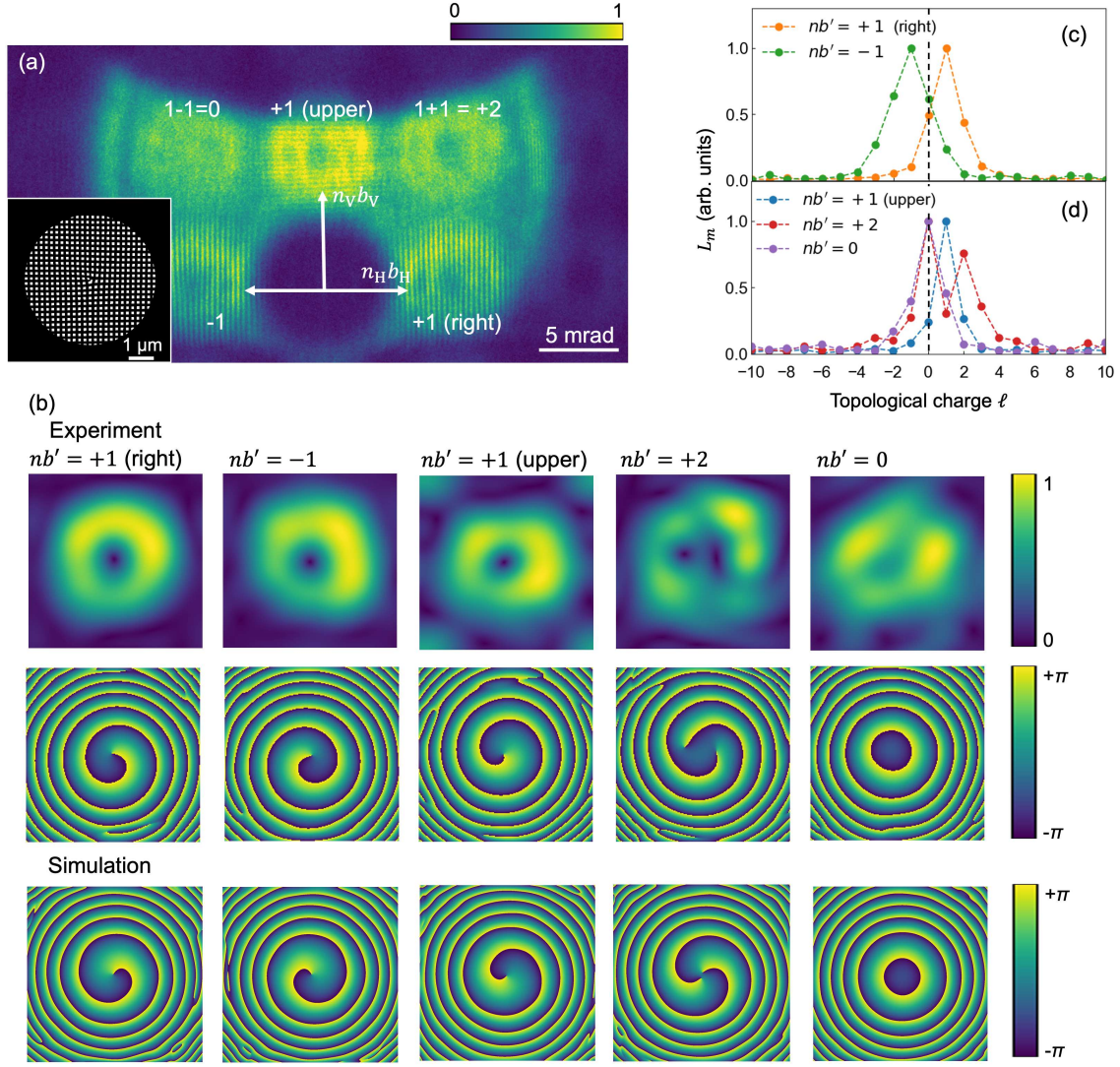


Figure 2. (a) Hologram pattern from the fork grating with $b_H = 1$ and $b_V = 1$. The inset shows a schematic of the fork grating. (b) $A(\rho_{fn}, \phi_{fn})$ (first row) and phase distribution (second row) of the vortex diffraction waves for $nb' = n_H b_H + n_V b_V = 0, \pm 1, +2$. Images in the third row present simulated phase patterns for these vortex diffraction waves. (c)(d) TC spectrum for each diffraction wave.

We also performed in-line holography for another fork grating constructed from two perpendicularly oriented $b = 1$ fork gratings, as illustrated in the inset of Fig. 2 (a). The transmission of this fork grating is given by

$$t(\rho, \phi) = \frac{1}{2} \left(1 + \text{sgn} \left[\sin \left(\frac{2\pi}{d} \rho \cos \phi + b_H \phi \right) \right] \right) \times \frac{1}{2} \left(1 + \text{sgn} \left[\sin \left(\frac{2\pi}{d} \rho \sin \phi + b_V \phi \right) \right] \right), \quad (10)$$

with topological numbers of two perpendicular gratings $b_H = 1$ and $b_V = 1$. This grating produces vortex waves as Bragg diffraction waves distributed over a square lattice. These diffraction waves are ideally expressed by a TC described as $\ell = nb' = n_H b_H + n_V b_V$, where n_H and n_V are the order of the Bragg diffraction along the horizontal and vertical directions, respectively; in one example, $(n_H, n_V) = (+1, +1)$ corresponds the $\ell = +2$ state. Figure 2 (a) shows the interference diffraction pattern from the fork grating, which is placed at $z_1 = 600 \mu\text{m}$ from the focal point and on the downside of the annular transmitting waves from the FZP. For $(n_H, n_V) = (\pm 1, 0)$ and $(n_H, n_V) = (0, +1)$, intensity modulation is observed along the horizontal and vertical orientations, respectively, and a fork-shaped pattern appears at the center. Meanwhile, for $(n_H, n_V) = (+1, \pm 1)$, modulation

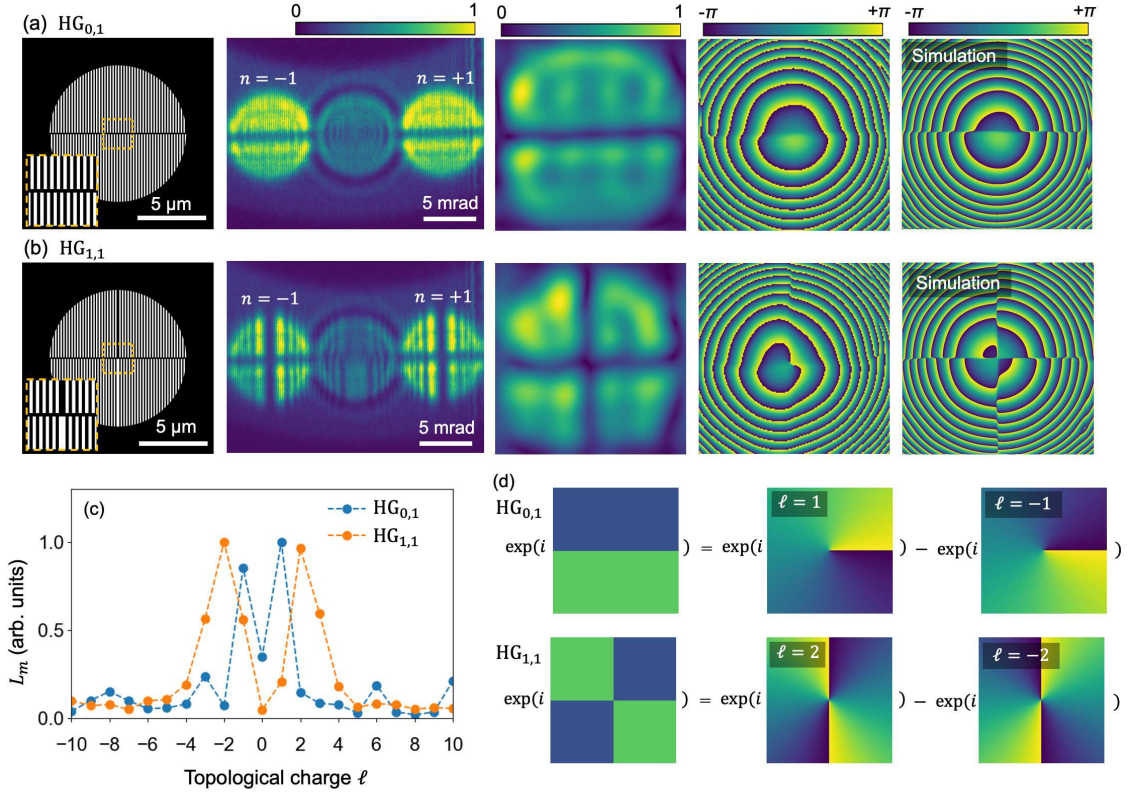


Figure 3. (a)(b) Inline holography for Hermite–Gauss states $HG_{0,1}$ and $HG_{1,1}$. Schematic of the gratings for producing $HG_{0,1}$ and $HG_{1,1}$ states (first column). Insets show enlarged views around the center of the gratings. Holographic images for the diffraction waves from these gratings (second column), $A(\rho_{fn}, \phi_{fn})$ (third column) and the phase distribution (fourth column) for the $n = +1$ diffraction, and the simulated phase distribution (fifth column). (c) TC spectra for the $HG_{0,1}$ and $HG_{1,1}$ states; figure (d) shows that these states can be decomposed into two LG states.

occurs along the diagonal diffraction, although a fork-shaped pattern is difficult to discern, even for $(n_H, n_V) = (+1, +1)$.

Spatial frequency filtering was performed for these diffractions. $A(\rho_{fn}, \phi_{fn})$ and the phase distributions for the $nb' = 0, \pm 1, +2$ diffraction waves are presented in the images in the first and second rows of Fig. 2 (b). We obtained a single spiral phase distribution for $nb' = \pm 1$, and the rotation angle was reversed depending on the sign of nb' . Notably, a clear double spiral phase distribution was obtained for the $nb' = +2$ diffraction despite the obscure interference intensity pattern; by contrast, a concentric circle pattern was obtained for $nb' = 0$. Simulated phase distributions for these Bragg diffraction waves are shown in the figures in the third row of Fig. 2 (b) and are in agreement with the experimental results. We also calculated the TC spectrum for these waves using Eq. (9); the results are shown in Figs. 2 (c) and (d). Well-defined peaks are observed at $\ell = \pm 1$ for $nb' = \pm 1$ and at $\ell = 0$ for $nb' = 0$ waves. For $nb' = +2$, contamination of the $\ell = 0$ mode to $\ell = +2$ mode is confirmed, similar to the diffraction wave from the $b = 2$ fork grating.

The present technique was also applied to Hermite–Gaussian ($HG_{u,v}$) modes. The gratings producing $HG_{0,1}$ and $HG_{1,1}$ states are illustrated in the images in the first column of Figs. 3 (a) and (b). Holographic images obtained for the diffraction waves from these gratings are shown in the images in the second column, where a horizontal intensity modulation appears for each wave. For both waves, stripes in the upper half of the diffraction pattern are out of phase with those in the lower half by π . We extracted $A(\rho_{fn}, \phi_{fn})$ and the phase distributions for the $n = +1$ order diffraction waves, as shown in the images in the third and fourth columns. We also simulated the phase distribution for these waves, as shown in images in the fifth column. The results were found to reasonably reproduce the experimental results. These results confirmed that phase inversion occurs at the horizontal center line for the $HG_{0,1}$ mode and at the horizontal and vertical center lines for the $HG_{1,1}$ mode. Figure 3 (c) shows the TC spectra for the $HG_{0,1}$ and $HG_{1,1}$ waves. Well-defined peaks are observed at $\ell = \pm 1$ and $\ell = \pm 2$ for $HG_{0,1}$ and $HG_{1,1}$, respectively, indicating that $HG_{0,1}$ ($HG_{1,1}$) mode can be decomposed into $\ell = \pm 1$ ($\ell = \pm 2$) LG modes as shown in Fig. 3 (d). It is known that transforming an HG mode to a LG mode and vice versa are possible²³. These results imply that our proposed technique is also effective for HG waves as well as for soft X-ray waves produced from arbitrary defects.

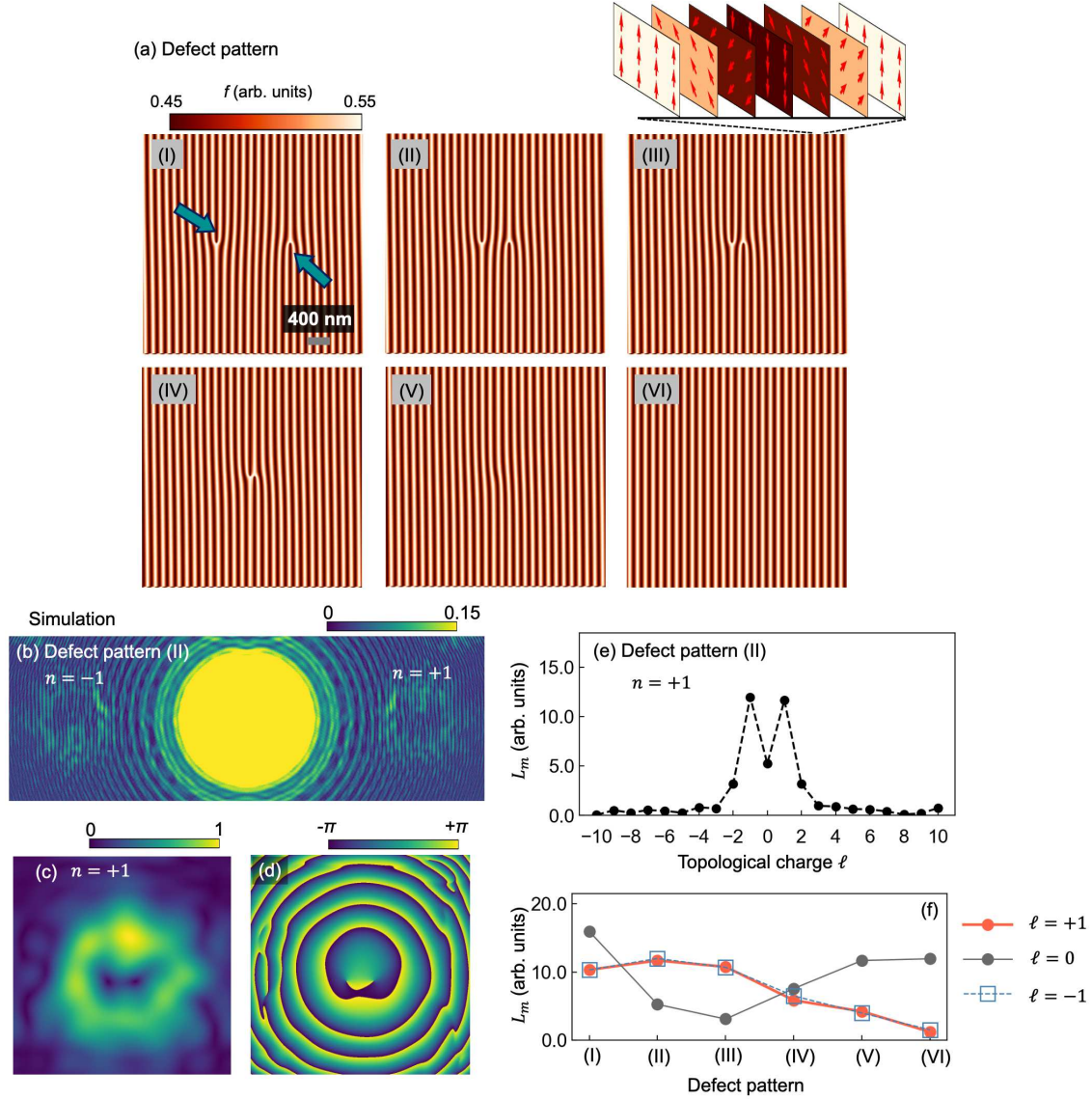


Figure 4. Simulation of inline holography for pair annihilation of edge dislocations in a helical magnetic texture. (a) (I)–(VI) Schematic of pair annihilation of the defects. Positive and negative edge dislocations (indicated by arrows in figure (I)) annihilate when they meet. (b) Holographic pattern calculated for $n = \pm 1$ diffraction from defect pattern II. (c) $A(\rho_{fn}, \phi_{fn})$, (d) phase distribution, and (e) TC spectrum for the $n = +1$ diffraction wave. (f) L_m of $\ell = \pm 1, 0$ for the $n = +1$ diffraction wave generated from each defect pattern.

Simulation of inline holography for dynamics of topological defects

Finally, we propose a practical application of our inline holography measurement to characterize the dynamics of topological defects in a magnet. Topological defects, such as edge dislocations (as shown in Fig. 4 (a)), have been commonly observed in several magnetic textures, including ferromagnetic stripe, helical, and skyrmion domain structures. Previous studies have reported the dynamics of topological defects in these magnetic textures under thermal fluctuation or a magnetic field^{17,27–29}.

Here, we simulated an inline holography experiment for pair annihilation of magnetic edge dislocations in a helical magnetic lattice, which is suggested by the calculation in Ref.²⁹. Figure 4 (a) illustrates positive and negative edge dislocations (with topological numbers $b = \pm 1$) in a helical magnetic lattice with a pitch of 120 nm. These two defects annihilate each other when they meet. We set the X-ray absorption to $f_{\uparrow} = 0.55$ for the magnetic moments pointing upward and to $f_{\downarrow} = 0.45$ for those pointing downward so that the XMCD signal $(f_{\uparrow} - f_{\downarrow}) / (f_{\uparrow} + f_{\downarrow})$ was comparable to the typical XMCD value for a transition-metal magnet at the L_{III} absorption edge (i.e., $(f_{\uparrow} - f_{\downarrow}) / (f_{\uparrow} + f_{\downarrow}) = 0.1$). For the outside of the sample, the X-ray

absorption was set to $f_{\text{outside}} = 0.02$. The simulated experimental geometry is the same as that shown in Fig. 1 (a), where the samples are placed at $z_1 = 600 \mu\text{m}$ from the focal point. Figure 4 (b) shows the calculated holographic image for diffraction waves with $n = \pm 1$ generated from defect pattern II, as obtained using the scaled FFT method²⁶. $A(\rho_{fn}, \phi_{fn})$ and the phase distribution for the $n = +1$ diffraction are obtained by spatial frequency filtering, as shown in Figs. 4 (c) and (d). The phase distribution clearly contains two singularities around the center, around which the phase locally rotates along the opposite direction, indicating that $\ell = \pm 1$ modes are generated from the positive and negative edge dislocations, respectively. The TC spectrum for the diffraction wave (shown in Fig. 4 (e)) clearly shows that the diffraction wave is decomposed to mainly $\ell = \pm 1$ modes as well as the $\ell = 0$ mode, which reflects the topological number of defect pattern II.

Figure 4 (f) shows the spectrum amplitude L_m of $\ell = 0, \pm 1$ modes for the diffraction wave generated from each defect pattern. When the two defects are far from each other (as shown in Fig. 4 (a)-I), the L_m of $\ell = 0$ mode is large compared with the L_m of the $\ell = \pm 1$ modes. As the defects approach the center, rotational phase components of the magnetic texture increase in the X-ray irradiation area, which results in an increase of the $\ell = \pm 1$ modes and a decrease of the $\ell = 0$ mode of the diffraction wave. As they approach further, the $\ell = 0$ mode increases again, with a concomitant decrease of the $\ell = \pm 1$ modes, reflecting the cancellation of the phase components of the $b = \pm 1$ defects. Finally, only the $\ell = 0$ mode wave is generated when the defects totally disappear. The dependence shown in Fig. 4 (f) represents the changes of the topological number on the magnetic texture associated with pair annihilation of the topological defects. Thus, acquiring the changes of the spectrum amplitude L_m enables the dynamics of topological defects in magnetic textures to be investigated.

Summary

We demonstrated inline holography experiments for soft X-ray vortex beams produced by several types of optical gratings. After analyzing the obtained holographic images, the TC of the LG vortex waves is successfully extracted, which reflect the topological numbers of the gratings, as well as the HG waves. In addition, we presented a simulation of the practical application of inline holography technique for pair annihilation of magnetic edge dislocations in a helical magnetic lattice. These results imply that the present technique can be used as an effective probe for the dynamics of topological defects on several types of magnetic textures.

Methods

Soft X-ray inline holography experiments were performed at beamlines BL-13A and BL-16A of the Photon Factory, KEK, Japan. The incident X-rays were focused via a FZP with outer and center beam-stopper radii of $60 \mu\text{m}$ and $30 \mu\text{m}$, respectively. The X-ray wavelength was tuned at $\lambda = 1.6 \text{ nm}$, which ideally resulted in a focal length of 1.5 mm . The first order diffraction from the FZP was selected by an OSA with a radius of $5 \mu\text{m}$ positioned in the vicinity of the focal point. Interference patterns were recorded using an in-vacuum CCD camera (Teledyne Princeton PMI2048, 2048×2048 pixels, pixel size $13 \mu\text{m}$). Fork gratings used in the present study were made from Ta metal with a thickness of 300 nm deposited onto a membrane of Si_3N_4 .

References

1. Shen, Y. *et al.* Optical vortices 30 years on: OAM manipulation from topological charge to multiple singularities. *Light. Sci. & Appl.* **8**, 1, DOI: <https://www.nature.com/articles/s41377-019-0194-2> (2019).
2. Grier, D. G. A revolution in optical manipulation. *Nature* **424**, 810, DOI: <https://www.nature.com/articles/nature01935> (2003).
3. Xiaodong, Q., FanGshu, L., Wuhong, Z., Zhihan, Z. & Lixiang, C. Spiral phase contrast imaging in nonlinear optics: seeing phase objects using invisible illumination. *Opt. Soc. Am.* **5**, 208, DOI: <https://www.osapublishing.org/optical/abstract.cfm?uri=optica-5-2-208> (2018).
4. Fujita, H. & Sato, M. Ultrafast generation of skyrmionic defects with vortex beams: Printing laser profiles on magnets. *Phys. Rev. B* **95**, 054421, DOI: <http://dx.doi.org/10.1103/PhysRevB.95.054421> (2017).
5. Yang, W., Yang, H., Cao, Y. & Yan, P. Photonic orbital angular momentum transfer and magnetic skyrmion rotation. *Opt. Express* **26**, 8778, DOI: <https://www.osapublishing.org/oe/fulltext.cfm?uri=oe-26-7-8778&id=384961> (2018).
6. Polyakov, O., Gonoskov, I. A., Stepanyuk, V. S. & Gross, E. K. U. Generation of magnetic skyrmions by focused vortex laser pulses. *J. Appl. Phys.* **127**, 073904, DOI: <https://aip.scitation.org/doi/10.1063/1.5140673> (2020).
7. Peele, A. G. *et al.* X-ray phase vortices: theory and experiment. *J. Opt. Soc. Am. A* **21**, 1575–1584, DOI: <http://josaa.osa.org/abstract.cfm?URI=josaa-21-8-1575> (2004).
8. Sakdinawat, A. & Liu, Y. Soft-x-ray microscopy using spiral zone plates. *Opt. letters* **32**, 2635, DOI: <https://www.osapublishing.org/ol/abstract.cfm?uri=ol-32-18-2635> (2007).

9. Sasaki, S. & McNulty, I. Proposal for Generating Brilliant X-Ray Beams Carrying Orbital Angular Momentum. *Phys. Rev. Lett.* **100**, 124801, DOI: <https://journals.aps.org/prl/abstract/10.1103/PhysRevLett.100.124801> (2008).
10. Bahrtdt, J. *et al.* First Observation of Photons Carrying Orbital Angular Momentum in Undulator Radiation. *Phys. Rev. Lett.* **111**, 034801, DOI: <http://dx.doi.org/10.1103/PhysRevLett.111.034801> (2013).
11. Takahashi, Y. *et al.* Bragg x-ray ptychography of a silicon crystal: Visualization of the dislocation strain field and the production of a vortex beam. *Phys. Rev. B* **87**, 121201, DOI: <https://link.aps.org/doi/10.1103/PhysRevB.87.121201> (2013).
12. Nakao, H. *et al.* Attempt to generate x-ray beam carrying orbital angular momentum in photon factory. *AIP Conference Proc.* **2054**, 060035, DOI: <https://doi.org/10.1063/1.5084666> (2019).
13. Lee, J., Alexander, S., Kevan, S., Roy, S. & McMorrnan, B. Laguerre–Gauss and Hermite–Gauss soft X-ray states generated using diffractive optics. *Nat. Photonics* **13**, 205, DOI: <https://www.nature.com/articles/s41566-018-0328-8> (2019).
14. Kohmura, Y. *et al.* X-ray microscope for imaging topological charge and orbital angular momentum distribution formed by chirality. *Opt. Express* **28**, 24115, DOI: <https://www.osapublishing.org/oe/fulltext.cfm?uri=oe-28-16-24115&id=433986> (2020).
15. Woods, J. S. *et al.* Switchable X-ray Orbital Angular Momentum from an Artificial Spin Ice. *Phys. Rev. Lett.* **126**, 117201, DOI: <http://dx.doi.org/10.1103/PhysRevLett.126.117201> (2021).
16. Masaya, U., Yoshinori, O., Yoshio, M. & Yoshinori, T. Real-Space Observation of Helical Spin Order. *Science* **311**, 359, DOI: <https://science.sciencemag.org/content/311/5759/359> (2006).
17. Rajeswari, J. *et al.* Filming the formation and fluctuation of skyrmion domains by cryo-Lorentz transmission electron microscopy. *Proc. Natl. Acad. Sci.* **112**, 14212, DOI: <http://www.pnas.org/content/112/46/14212.abstract> (2015).
18. Nakajima, H., Kotani, A., Mochizuki, M., Harada, K. & Mori, S. Formation process of skyrmion lattice domain boundaries: The role of grain boundaries. *Appl. Phys. Lett.* **111**, 192401, DOI: <https://doi.org/10.1063/1.4991791> (2017).
19. Paterson, G. W. *et al.* Order and disorder in the magnetization of the chiral crystal CrNb₃S₆. *Phys. Rev. B* **99**, 224429, DOI: <http://dx.doi.org/10.1103/PhysRevB.99.224429> (2019).
20. Birch, M. T. *et al.* Real-space imaging of confined magnetic skyrmion tubes. *Nat. Commun.* **11**, 1726, DOI: <https://doi.org/10.1038/s41467-020-15474-8> (2020).
21. Zheng, F. *et al.* Experimental observation of chiral magnetic bobbars in B20-type FeGe. *Nat. Nanotechnol.* **13**, 451, DOI: <https://doi.org/10.1038/s41565-018-0093-3> (2018).
22. Li, Y. *et al.* Tunable terahertz oscillation arising from Bloch-point dynamics in chiral magnets. *Phys. Rev. Res.* **2**, 033006, DOI: <http://dx.doi.org/10.1103/PhysRevResearch.2.033006> (2020).
23. Beijersbergen, M., Allen, L., van der Veen, H. & Woerdman, J. Astigmatic laser mode converters and transfer of orbital angular momentum. *Opt. Commun.* **96**, 123, DOI: [https://doi.org/10.1016/0030-4018\(93\)90535-D](https://doi.org/10.1016/0030-4018(93)90535-D) (1993).
24. Ishii, Y. *et al.* Soft-X-Ray Vortex Beam Detected by Inline Holography. *Phys. Rev. Appl.* **14**, DOI: <https://doi.org/10.1103/PhysRevApplied.14.064069> (2020).
25. Richard, N. *et al.* Correcting vortex splitting in higher order vortex beams. *Opt. Express* **22**, 9920, DOI: <https://www.osapublishing.org/oe/fulltext.cfm?uri=oe-22-8-9920&id=283592> (2014).
26. Bailey, D. H. & Swartztrauber, P. N. The fractional fourier transform and applications. *Soc. for Ind. Appl. Math.* **33**, 389, DOI: <https://epubs.siam.org/doi/pdf/10.1137/1033097> (1991).
27. Fin, S. *et al.* Straight motion of half-integer topological defects in thin Fe-N magnetic films with stripe domains. *Sci. Reports* **8**, 9339, DOI: <https://doi.org/10.1038/s41598-018-27283-7> (2018).
28. Pamyatnykh, L. A., Filippov, B. N., Agafonov, L. Y. & Lysov, M. S. Motion and Interaction of Magnetic Dislocations in Alternating Magnetic Field. *Sci. Reports* **7**, 18084, DOI: <https://doi.org/10.1038/s41598-017-18033-2> (2017).
29. Dussaux, A. *et al.* Local dynamics of topological magnetic defects in the itinerant helimagnet FeGe. *Nat. Commun.* **7**, 12430, DOI: <https://doi.org/10.1038/ncomms12430> (2016).

Acknowledgements

This work was partly supported by JSPS KAKENHI with project Nos. JP17K05130, JP19H04399, JP19K23590, JP20K20107, and JP20H04458 and by MEXT Quantum Leap Flagship Program (MEXT Q-LEAP) Grant Number JPMXS0118068681, and

by Research Foundation for Opto-Science and Technology. This work is also partially supported by PRESTO (JPMJPR177A), CREST(JPMJCR1861), Japan Science and Technology Agency (JST). Soft X-ray scattering work was performed under the approval of the Photon Factory Program Advisory Committee (Proposal Nos. 2018S2-006, 2019G590, and 2019PF-22).

Author contributions

Y.I., H.N., and Y.Y. conducted the experiments. Y.I. analyzed the results and carried out calculations of the scaled FFT. The results were discussed and interpreted by Y.I., M.M., H.N., Y.W., T.A., and Y.Y. All authors reviewed the manuscript.